



# Segmentation and three-dimensional reconstruction of lesions using the automated breast volume scanner (ABVS)

Teresa Araújo<sup>1,2</sup>

Momen Abayazid<sup>1,3\*</sup>

Matthieu J. C. M. Rutten<sup>4</sup>

Sarthak Misra<sup>1,5</sup>

<sup>1</sup>Department of Biomechanical Engineering, University of Twente, P. O. Box 217, 7500 AE, Enschede, Overijssel, Netherlands

<sup>2</sup>Faculty of Engineering of University of Porto, Rua Dr. Roberto Frias, 4200-465, Porto, Portugal

<sup>3</sup>Department of Radiology, Brigham and Women's Hospital and Harvard Medical School, 75 Francis Street, Boston, MA 02119, USA

<sup>4</sup>Department of Radiology, Jeroen Bosch Hospital, Nieuwstraat 34, 5211 NL's-Hertogenbosch, The Netherlands

<sup>5</sup>Department of Biomedical Engineering, University of Groningen and University Medical Centre Groningen, Antonius Deusinglaan 1, 9713 AV, Groningen, The Netherlands

\*Correspondence to: Momen Abayazid, Department of Biomechanical Engineering, University of Twente, P. O. Box 217, 7500 AE, Enschede, Overijssel, Netherlands. Email: mabayazid@bwh.harvard.edu  
Supporting info item

## Abstract

**Background** Ultrasound is an effective tool for breast cancer diagnosis. However, its relatively low image quality makes small lesion analysis challenging. This promotes the development of tools to help clinicians in the diagnosis.

**Methods** We propose a method for segmentation and three-dimensional (3D) reconstruction of lesions from ultrasound images acquired using the automated breast volume scanner (ABVS). Segmentation and reconstruction algorithms are applied to obtain the lesion's 3D geometry. A total of 140 artificial lesions with different sizes and shapes are reconstructed in gelatin-based phantoms and biological tissue. Dice similarity coefficient (DSC) is used to evaluate the reconstructed shapes. The algorithm is tested using a human breast phantom and clinical data from six patients.

**Results** DSC values are  $0.86 \pm 0.06$  and  $0.86 \pm 0.05$  for gelatin-based phantoms and biological tissue, respectively. The results are validated by a specialized clinician.

**Conclusions** Evaluation metrics show that the algorithm accurately segments and reconstructs various lesions. Copyright © 2016 John Wiley & Sons, Ltd.

**Keywords** ultrasound; computer-assisted diagnosis; breast lesion segmentation; three-dimensional reconstruction

## Introduction

Breast cancer is one of the main mortality causes for women worldwide (1) and the first cause of female death by cancer (2). Although the number of cases is decreasing in developed countries, breast cancer occurrence is still increasing globally (3). Breast cancer is most effectively treated when detected at an early stage (4), resulting in at least 40% death rate reduction (5). Therefore, there is need for effective diagnostic systems to enable prevention, detection and monitoring of breast cancer. Several imaging techniques can be used for breast cancer detection and diagnosis. Some examples are mammography, ultrasound (US) imaging and magnetic resonance imaging (1). Mammography has been the most commonly used screening modality (5,6).

Accepted: 12 July 2016

Nevertheless, there are limitations associated with this technique: 1) lesions can be masked by a dense parenchyma (7); 2) it has low specificity, leading to unnecessary biopsies (8); and 3) the ionizing radiation can be harmful to the patient (5).

Breast MR imaging is commonly used for lesion diagnosis. Its use is limited to women who are at high risk for developing breast cancer, and also for monitoring treatment. Breast US imaging is a helpful technique to complement mammography (9–11). US images can help to accurately discriminate benign and malignant masses (10,12). Furthermore, US can be more sensitive in patients with dense breast tissues (13). The accuracy rate of US imaging for cysts diagnosis is significantly higher than mammography imaging. This helps reducing the number of unnecessary biopsies (12). In addition, this modality is non-invasive, cost-effective, has no known side-effects and provides real-time diagnostic capability. However, breast US images usually have poor quality due to speckle noise, low contrast, blurred edges and shadow effect (14). The analysis of US images by clinicians can be challenging (15,16).

Besides imaging properties, correct diagnosis also depends on the clinician. The assessment of the lesion shape is important for the diagnosis. Nevertheless, manually sketching a breast tumor contour is significantly time-consuming. Also, interobserver variation results in different analyses even among well-trained clinicians (17). This reality promotes the development of computer-aided diagnosis (CAD) systems to help clinicians in the diagnosis (18). CAD systems allow reduction of the operator-dependent nature of US imaging-based diagnosis, increasing its reproducibility. The second opinion provided by the CAD system can increase diagnostic accuracy and may speed-up diagnostic reading.

US CAD systems usually include four stages: image pre-processing, segmentation, feature extraction and selection, and classification. Image segmentation is a fundamental step that separates the lesion from the background and other imaging artifacts. A proper segmentation preserves important lesion characteristics such as shape and texture. Shape and volume of the lesion are of great importance in the diagnostic process (19). Volume information can also be used to trace the lesion variant state in clinical applications (20,21). This knowledge can be used to adapt patient treatment. Accurate lesion segmentation and three-dimensional (3D) reconstruction can improve breast cancer detection rate.

## Related work

Several segmentation methods for breast lesions on US images were proposed. Segmentation algorithms

functioning heavily depends on the image pre-processing and segmentation methods used. Several authors used histogram thresholding for segmentation (22–26). Horsch *et al.* (22) pre-processed images using cropping, median filtering and multiplication by a Gaussian constraint function. The approach was based on maximizing a utility function over partition margins defined through thresholding. However, the determination of the center, width and height of lesions is not automatic. Chen *et al.* (23) pre-processed regions of interest (ROIs) with median filtering and unsharp filtering. Binarization was performed by histogram thresholding. Yeh *et al.* (26) used adaptive thresholding and disk expansion to select and refine the object. Histogram thresholding is a simple and fast method. Still, binarization in non-bimodal histograms lacks precision, resulting in imprecise boundaries. This technique can be combined with methods like morphological operations, disk expansion and function optimization to refine the contour.

Model-based approaches are also used for breast US images segmentation. These include active contours (27,28), level-sets (29,30) and Markov random filters (31,32). Madabhysbi *et al.* (27) used active contours. Seed points were found using a method based on the empirical rules used by radiologists to detect breast lesions. Probabilistic classification and region growing retrieved an initial contour. A deformable model using the image gradient was then applied. Boukerroui *et al.* (31) applied Markov random filters. The adaptive characteristics were controlled by a weighting function accounting for both local and global statistics. Model-based approaches are noise resistant. However, the iterative process is time-consuming. Also, the algorithm can stop on local minima states. Furthermore, many models are semi-automatic and require pre-labeled ROIs or manually initialized contours.

Watershed-based algorithms were applied to US breast images (33,34). Gómez *et al.* (33) pre-processed and multiplied images by a constraint Gaussian function. Marker-controlled watershed transformation was used to find potential lesion boundaries. Lesion contour was detected using an average radial derivative function. The method requires a heuristic estimation of the best thresholding of markers. Zhang *et al.* (34) used fuzzy logic theory and transformed the US image into fuzzy domain. An iterative method was used to find the threshold. Watershed segmentation was applied on the binary image to get the final tumor boundary. Watershed approaches show promising results. However, the over-segmentation problem is not completely solved.

Machine learning methods are recurrent in US breast lesion segmentation (35–39). Drukker *et al.* (35) trained a Bayesian neural network with texture, gradient and acoustic information. Seed points were found in the

gradient image and region growing was used to obtain the candidate regions. However, it is not robust for non-compact or rounded lesions. Also, the number of hidden layers for the neural network is empirically defined. In Su *et al.* (37) the initial lesion contour was obtained with a self-organizing map neural network and a modified Normalized Cut approach. Active contours refined the segmentation. The method lacks post-processing to reduce shadow influence in ROI detection and lesion segmentation. Liu *et al.* (39) combined Support Vector Machines with textural features. Although machine learning methods show satisfactory results, both selection of a good set of features and classifier training are time-consuming. Also, training depends on the database.

The above methods were applied in 2D US images. Other algorithms considered the 3D space (19–21,40,41). Chen *et al.* (21) used active contour modeling for contour detection. During the deformation process, edge information was added as an image feature to define the external force. This prevents the snake stopping in false positions. Huang *et al.* (19) used 3D region growing to obtain the tumor contour. Voxel nearest neighbor, Wiener and unsharp filters were applied to pre-process the images. Shadow regions were reduced with post-processing. The algorithm is very time-consuming. In Chang *et al.* (42) images were pre-processed with morphological operators. A modified watershed algorithm was used for semi-automatic contour extraction. In Kuo *et al.* (40) the initial contour was estimated using radial gradient index segmentation. An active contour model with a dynamic stopping criteria was then used. Nevertheless, a seed point in the center of the lesion must be defined manually. Also, the method is not optimized for US.

Most of the algorithms developed depend on a manual ROI selection (23,24,28,29,33,36) (in 2D) or a volume of interest (VOI) (19,21,42) (in 3D) in order to produce viable results (25). Even when a ROI is not clearly stated to be needed, input US images usually have little non-lesion area (20,27,31,41). VOI manual selection is commonly done by selecting ROIs in the first, middle and last 2D slices of the lesion. Also, the referred algorithms did not appear to return a reconstructed shape of the lesion. The lesion 3D shape and volume are of great interest to the clinicians.

## Contributions

In the current study, we develop a system that performs ultrasound scanning of various soft-tissue phantoms to segment and reconstruct different shapes of lesions. We focus mainly on breast lesions. An intensity-based segmentation method for breast lesions in a US image sequences is proposed. The principal technique applied is

histogram thresholding. After segmentation, the 3D connected components between slices are found, i.e. 3D objects. Artificial lesions are reconstructed in gelatin-based soft-tissue phantoms and biological tissue (chicken breast) to test the algorithm. The proposed segmentation and 3D reconstruction algorithm is also validated using a commercial breast phantom that is used to train clinicians for ultrasound biopsy procedures. This breast phantom has similar mechanical and visual properties of human breast tissue in US images, and it also contains amorphous lesions. Clinical patient data is also analyzed and the algorithm results validated by an experienced clinician. Furthermore, a Graphical User Interface (GUI) for the algorithm is proposed.

The major contributions of this work include:

- Development of an algorithm for lesion segmentation and 3D reconstruction in US image sequences. The main features of the algorithm are:
  - no requirement for VOI selection;
  - detection of lesions with different sizes and geometries;
  - reduced computation time.
- Development of a GUI to:
  - retrieve the 3D shape and volume of a lesion for clinicians;
  - localize structures in the environment for biopsy planning (43).
- Experimental evaluation of the proposed algorithm using soft-tissue phantoms and clinical patient data.

## Materials and Methods

A method for lesion segmentation and 3D reconstruction in US image sequences is proposed. Tests are performed in gelatin, biological tissue and commercial breast phantoms, as well as in clinical patient data. This section details the scanning procedure and the algorithm steps. The segmentation and reconstruction algorithm is fully implemented in MATLAB (R2015a, Mathworks Inc., Natick, USA). US image acquisition is performed using an in-made C++ algorithm.

### Ultrasound scanning

Phantoms and patient breasts are scanned using a Siemens Acuson S2000™ (Siemens AG, Erlangen, Germany) ultrasound device. US image sequences are

obtained using the Automated Breast Volume Scanner (ABVS) (Siemens Medical Solutions, Mountain View, CA, USA). The ABVS system is composed of a cage that contains a transducer (14LBV). The 14LBV transducer translates automatically using a linear stage with constant velocity. The system settings can be found in Table 1. An overall view of the setup design is available in Figure 1. Phantom US scans have a frame rate of 11 or 20 frames per second. The spatial resolution of each slice is  $720 \times 480$  pixels or  $720 \times 576$  pixels. The number of 2D slices for clinical US scans is 318 and the resolution  $565 \times 698$  pixels.

## Segmentation and 3D reconstruction

The main steps of the segmentation and reconstruction algorithm are shown in Figure 2. In this work, an intensity-based segmentation is proposed. All US 2D slices are segmented separately. Figure 3 illustrates the application of the approach used. Prior to segmentation, dark regions that result from the width difference between the phantoms and the transducer are removed. An algorithm that automatically detects the phantom region

**Table 1** ABVS system properties. FB stands for frequency bandwidth and MDP for maximum display depth. Voxel size of the system along the planes is shown in the following order: axial, lateral and elevation planes

Velocity	Width	MDP
1.55 or 2.55 mm/s	154 mm	60 mm
No. of elements	FB	Voxel size
768	5–14 MHz	$0.09 \times 0.16 \times 0.44 \text{ mm}^3$

is developed. Projections are performed in both horizontal and vertical directions to detect high intensity transitions. Then, the projections' peaks are detected. The region of interest lies between the peaks.

Pre-processing is used to remove speckle noise and adjust contrast. The red channel of the RGB image is selected since it generally has greater contrast between objects and background. Speckle noise is removed by applying a median filter with kernel size of 5. The image is inverted if the object is brighter than the background. Image contrast is adapted using linear histogram stretching. First, the background intensity level,  $\zeta$ , is computed. Then, a mapping function is determined based on  $\zeta$ .

Background intensity determination is described in Algorithm 1 and illustrated in Figure 4-I.

---

### Algorithm 1. Algorithm for background intensity determination

---

**Require:** *image* and *type\_image* {*phantom* / *breast*}

*back\_image*  $\leftarrow$  MedianFilter(*image*) {large size}

*back\_image*  $\leftarrow$  RemoveBorders(*back\_image*)

**if** *type\_image* = *phantom* **then**

*back\_image*  $\leftarrow$  RoundToDecimalPoint(*back\_image*)

$\zeta \leftarrow \text{mode}(\text{back\_image})$

**else**

$\mu \leftarrow \text{mean}(\text{back\_image})$

*poly\_reg*  $\leftarrow$  PolynomialRegression(*back\_image*) {10<sup>th</sup> degree}

$\zeta \leftarrow \text{DetectFirstPeak}(\text{poly\_reg})$  with intensity  $> 0.7 \times \mu$

**end if**

**return**  $\zeta$

---

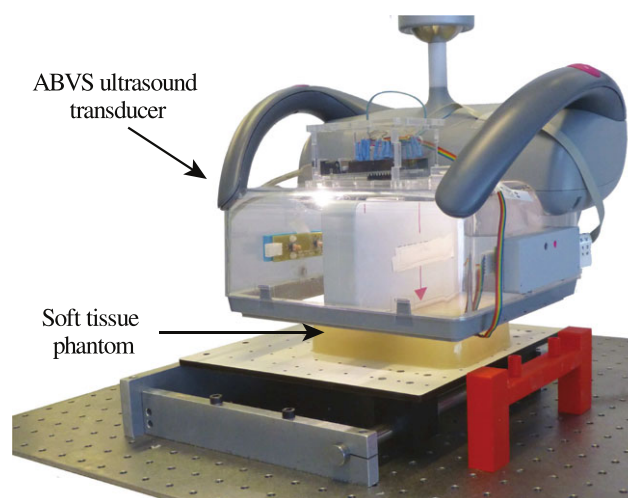


**Figure 1.** The experimental setup used for phantom screening, showing the Automated Breast Volume Scanner (ABVS) and a gelatin-based soft-tissue phantom



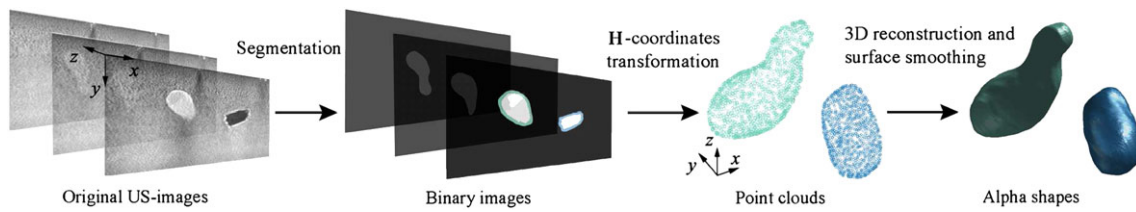


Figure 2. Main steps of the segmentation and three-dimensional (3D) reconstruction algorithm. First, the stack of ultrasound images is segmented. The resulting binary connected components are then transformed to 3D space using the transformation matrix  $H$ . Finally, the alpha shapes of the obtained 3D point clouds are computed and the object surfaces smoothed

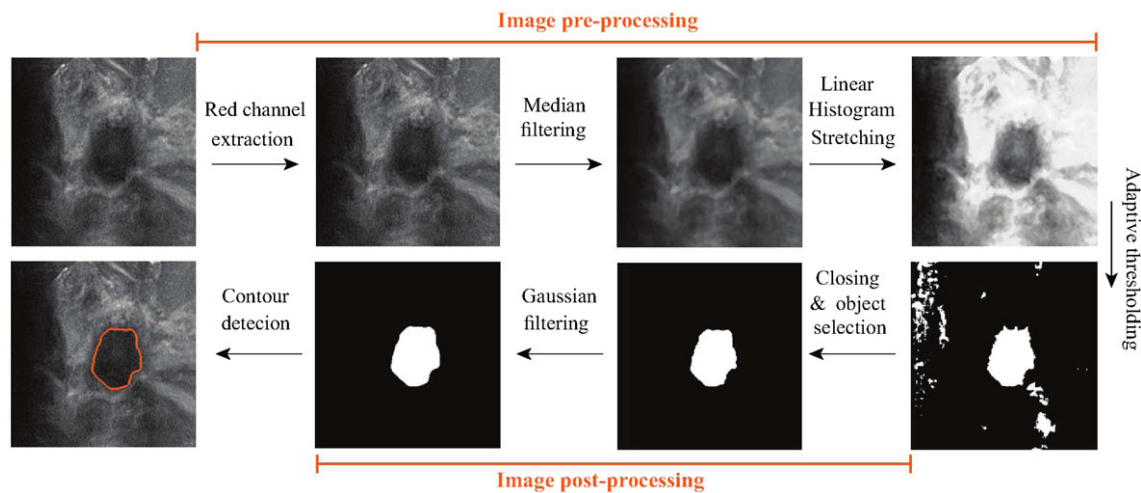


Figure 3. Segmentation algorithm steps applied to a patient breast lesion: image pre-processing, binarization and post-processing. First, the red channel of the image is extracted since it generally shows greater contrast between objects and background. Then, a median filter is applied in order to remove speckle noise. This is followed by a linear histogram stretching to adjust contrast. Image binarization is then performed using an adaptive thresholding method. The resulting binary image is post-processed using closing morphological operation to fill possible holes in the lesion and Gaussian filtering to smooth the contour. (Note that, although only the region containing the lesion is shown, the whole image is considered during segmentation.)

The mapping function ( $g(f)$ ) is determined based on the estimated  $\zeta$ :

$$g(f) = \begin{cases} \frac{(g_b - g_a)}{f_b - f_a}(f - f_a) + g_a, & \text{if } f_a \leq f \leq f_b \\ \frac{(g_c - g_b)}{f_c - f_b}(f - f_b) + g_b, & \text{if } f_b \leq f \leq f_c \end{cases} \quad (1)$$

where  $f$  is the input intensity value,  $g$  the output intensity value,  $f_a = 1$ ,  $f_b = 1.1 \times \zeta$ ,  $f_c = 1$ ,  $g_a = 1$ ,  $g_b = 0.85$  and  $g_c = 1$ . An example of a mapping function is shown in Figure 4-II. The mapping function adjusts the contrast between objects and background by compressing high intensity values (see Figure 4-III). If  $\zeta = g_b$ , no compression is performed.

The adjusted image is then binarized using an adaptive method. Threshold values for each pixel are computed based on the local neighborhood. Local threshold values are found using the mean of the local intensity

distribution (44,45). Binarization steps (illustrated in Figure 5) are described in Algorithm 2. The threshold default value is determined by trial and error experimentation. Results are successful in most of the cases.

---

**Algorithm 2** Algorithm for binarization using adaptive thresholding

---

**Require:** Pre-processed image: *original\_image*  
 $w \leftarrow \text{width}(\text{original\_image})$   
 $h \leftarrow \text{height}(\text{original\_image})$   
 $\text{average\_image} \leftarrow \text{AverageFilter}(\text{original\_image})$   
 $\{\text{filter size} = 0.25 \times \min(w, h)\}$   
 $\text{diff\_image} \leftarrow (\text{average\_image} - \text{original\_image})$   
 $\text{hist} \leftarrow \text{histogram}(\text{diff\_image})$   
 $\text{mean\_hist} \leftarrow \text{mean}(\text{hist})$   
 $\text{std\_hist} \leftarrow \text{std}(\text{hist})$   
 $T \leftarrow \text{mean\_hist} + 1.75 \times \text{std\_hist}$  {default value}  
 $\text{binary\_image} \leftarrow \text{original\_image} > T$   
**return** *binary\_image*

---

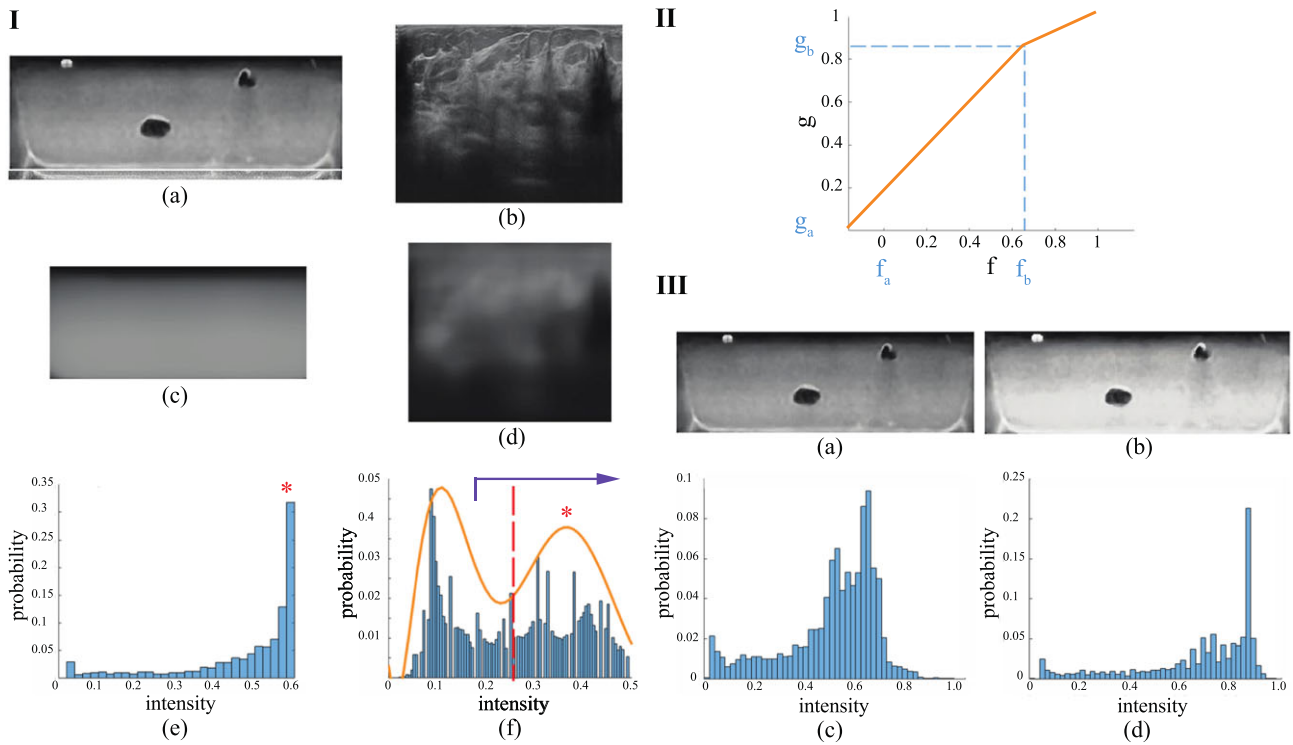


**Figure 4. Linear histogram stretching steps.** I: Background intensity level determination. (a) and (b): US images from phantom and patient breast, respectively; (c) and (d): (a) and (b) after median filter application and dark borders removal, respectively; (e) and (f): histograms of (c) and (d), respectively. Detected peaks corresponding to the background intensity values ( $\zeta$ ) are shown (red \*). In (f), the mean intensity value ( $\mu$ ) (dashed red line), the polynomial regression of the histogram (orange curve) and the intensity range for peak search ( $[0.7 \times \mu \ 1]$ ) (purple arrow) are also visible.  $\zeta$  determination differs for the two types of images due to the highly nonhomogeneous and noisy nature of patient breast images. In phantom images, the mode of the histogram is used to find the background intensity level. For patient breast images, the mean is computed. A polynomial regression of the histogram is performed to avoid noise interference.  $\zeta$  is the first peak detected within the referred range. II: Mapping function for case I-(a), where  $\zeta = 0.6$ . The function  $g(f)$  is defined according to Equation (1):  $f_a = 1$ ,  $f_b = 1.1 \times \zeta$ ,  $f_c = 1$ ,  $g_a = 1$ ,  $g_b = 0.85$  and  $g_c = 1$ . III: Application of the mapping function II to case I-(a). (a): Phantom US image; (b): (a) after linear histogram stretching; (c) and (d): histograms of (a) and (b), respectively

Finally, the binarized image is post-processed. A morphological closing (disk, radius 3) is performed to remove holes that result from poor image quality and artifacts. A Gaussian filter ( $\sigma = 2.5$ ) is then applied to smooth the contour.

The stack of binary images containing the object of interest is reconstructed to 3D. First, all pixels are reorganized in the 3D space ( $x, y, z$ ) taking into account the position of the ABVS transducer with respect to time and the pixel scale. For that, the homogeneous transformation  $\mathbf{H}_n$  (Equation (2a)) is applied to the pixel ( $x_i, y_i$ ) in frame  $n$ . The resulting coordinates,  $\mathbf{P}_{i_n}$ , are obtained using Equation (2b).

$$\mathbf{H}_n = \begin{bmatrix} 0 & 0 & -1 & \lambda_n \\ -1 & 0 & 0 & 0 \\ 0 & 1 & 0 & 0 \\ 0 & 0 & 0 & 1 \end{bmatrix} \quad (2a)$$

$$\mathbf{P}_{i_n} = \mathbf{H}_n \times \begin{bmatrix} x_i \times \delta_x \\ y_i \times \delta_y \\ 0 \\ 1 \end{bmatrix} \quad (2b)$$

In Equation (2a),  $\lambda_n$  is the displacement of the slice  $n$  relative to the first slice of the stack, in mm. In Equation (2b),  $\delta_x$  and  $\delta_y$  (mm/pixel) are the width and height scales, respectively.

The transformation results in points organized in a 3D space, i.e. a 3D point cloud. Reconstruction is then performed by determining the alpha shape of the point cloud. Alpha shapes are a generalization of the convex hull of a set of points (46). An alpha shape is not necessarily convex nor connected. The behavior of the shape depends on a parameter  $\alpha$ : for  $\alpha = \inf$  the alpha shape is the convex hull of the point set; as the  $\alpha$  value gets lower, cavities are formed. If  $\alpha$  is too low, holes appear in the reconstruction. When  $\alpha$  is zero an empty shape is produced. In this work, the  $\alpha$

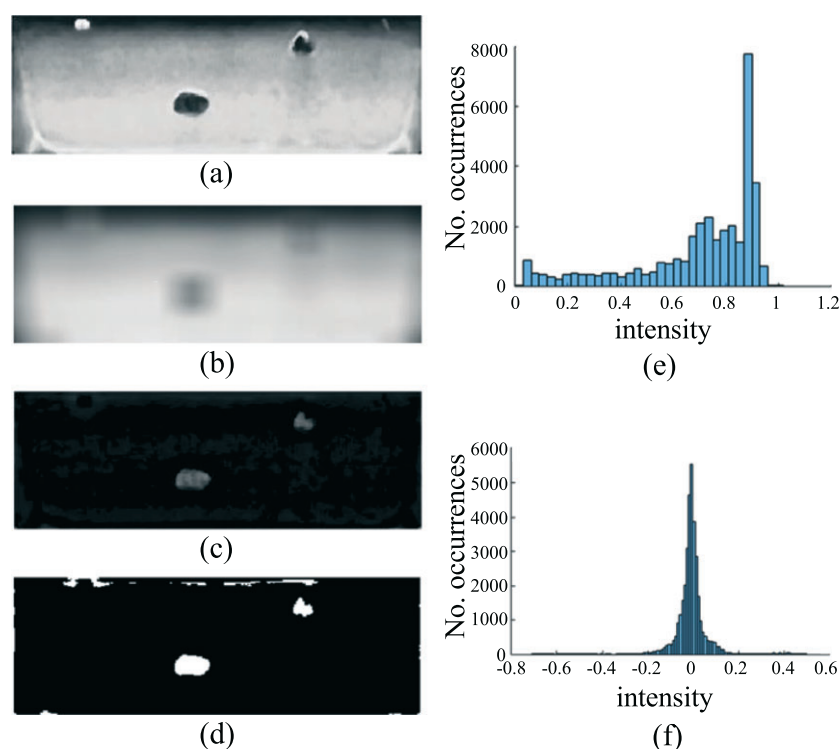


Figure 5. Steps of image binarization through adaptive thresholding using the mean of the local intensity distribution. (a): Linear stretched image; (b): image (a) after application of the average filter; (c): result of the subtraction (b) – (a); (d): resulting binarized image; (e) and (f): histograms of (b) and (c), respectively

value used for a certain object point cloud is the critical alpha, i.e. the smallest  $\alpha$  that produces an alpha shape that encloses all points. The overall shape of the reconstructed

objects is improved by applying a smoothing filter to the object surfaces (see Figure 6). The smoothing algorithm is based on (47,48) and was developed by (49).

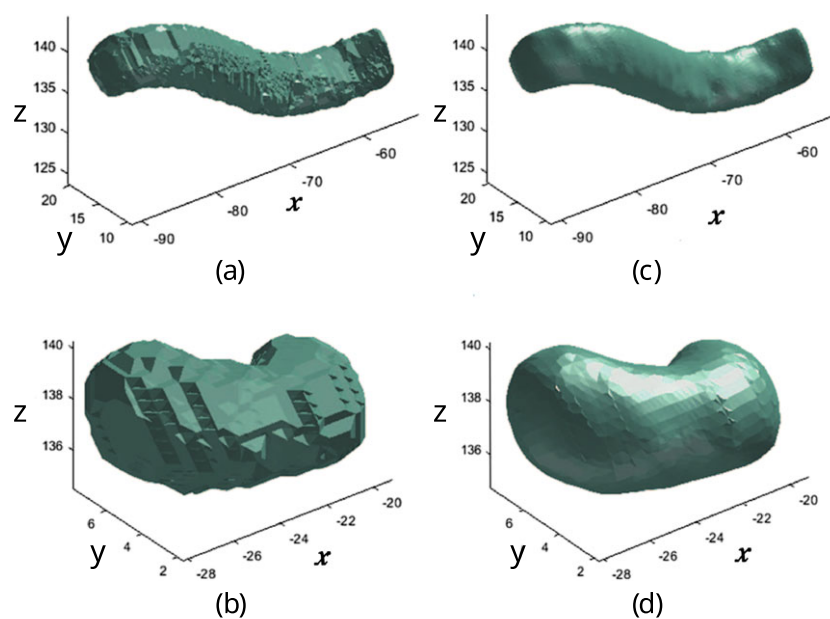


Figure 6. Smoothing of objects mesh surfaces. (a) and (b): object meshes before smoothing; (c) and (d): smoothed object meshes of (a) and (b), respectively. (axes units: mm)

## Reconstruction evaluation

The reconstructed object and the ground truth are compared. The evaluation is performed by: (1) registration of the point clouds to align the object with the ground truth; and (2) evaluation using the Dice similarity coefficient (DSC) and mean absolute distance (MAD) metrics.

Point cloud registration is performed using the iterative closest point (ICP) method (50). The algorithm estimates a rigid transformation that minimizes the distance between two point clouds (one object is fixed and the other is transformed). The two views must be close to each other, otherwise, the algorithm will probably stop at a local minimum (51). This problem can be solved by a pre-alignment of the two 3D shapes. For that, principal components analysis (PCA) is used. First, both objects are centered at the origin of the coordinate system using their centers of mass. Objects are then aligned by their major axes using PCA. However, using PCA results in a  $\pi$  rad ambiguity in the direction of the objects' principal axes. This can be solved by studying all the  $180^\circ$  rotations around their axes. Consequently, all combinations of one, two and three elements of  $\{rot_x, rot_y, rot_z\}$  are performed, where  $rot_x$ ,  $rot_y$  and  $rot_z$  denote the rotations of  $\pi$  rad around  $x$ ,  $y$  and  $z$  axes, respectively. This results in eight

possible alignments. In the end, the alignment with lowest root mean square error is chosen.

DSC and MAD evaluation metrics are calculated. DSC (52) is a spatial overlap index and is defined by:

$$DSC = \frac{2 \times V_{intersection}}{V_{object1} + V_{object2}} \quad (3)$$

where  $V_{object1}$  and  $V_{object2}$  are the volumes of the reconstructed and ground truth objects, respectively, while  $V_{intersection}$  is the volume of their intersection. DSC value ranges from 0 (no spatial overlap between the two objects) to 1 (complete overlap). MAD (53) is related to the average distance between the two surfaces. Both measures are efficiently calculated using the MeshValmet software. The general steps of the algorithms for determining these measures can be found in Ref (54). An algorithm is also developed to compute DSC values in MATLAB.

## Graphical User Interface (GUI)

A GUI for the proposed algorithm is developed. The GUI can be used to segment an US image sequence, select an object of interest (via mouse-click) and retrieve the object 3D shape (Figure 7). Segmentation parameters can be adjusted if needed. A preview of the 3D reconstructed

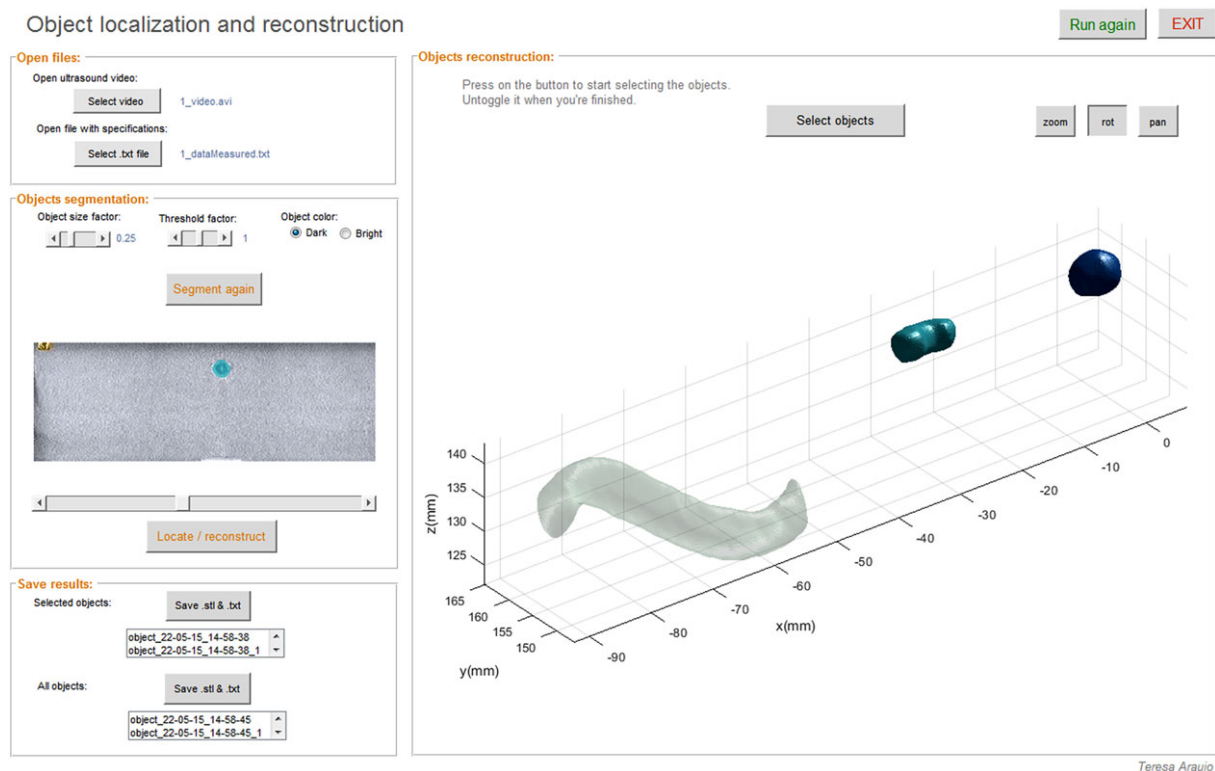


Figure 7. Design of the developed graphical user interface



object is shown. Objects can also be saved as *.stl* (stereolithography) files for further processing and evaluation. Clinicians can retrieve important information for the diagnosis, such as lesion 3D shape and volume. Furthermore, lesion localization can assist the clinician for biopsy planning. (Please refer to the accompanying video that demonstrates the experiments (Electronic Supplementary Material).)

## Experiments

Evaluation of the algorithm is performed by segmenting different object shapes in: (1) gelatin-based phantoms; (2) biological tissue (chicken) phantoms; (3) breast phantom; and (4) clinical patient data. The procedures for each type of data are discussed in this section.

**Case I: Gelatin-based phantoms:** Phantoms are prepared as described in (55), in order to mimic tissue properties (56–59). Targets and obstacles are prepared using a solution of 2% agar powder (m/m) (20768.292, VWR) in water. The solution is heated to 90 °C and poured into molds. Figure 8(a) and (b) shows a prepared phantom and a slice of the respective US scan. Objects with different shapes, sizes and positions are used to evaluate the generality of the algorithm.

**Case II: Biological tissue phantoms:** For phantom preparation, chicken breasts are submerged in gelatin (prepared as in Case I). Prior to this, agar objects are incorporated in the chicken through a incision along its major axis. An overall view of a biological tissue phantom and an example of an US image can be seen in Figure 8(c) and (d).

The object shapes used in Case I) are evaluated in biological tissue phantoms.

**Case III: Human breast phantom:** A commercial human breast phantom (CIRS, Norfolk, USA) is used. This phantom contains lesions of different sizes and shapes. Both dark and bright lesions are segmented and reconstructed. Figure 8(e) and (f) shows the breast phantom and a slice of the respective US scan.

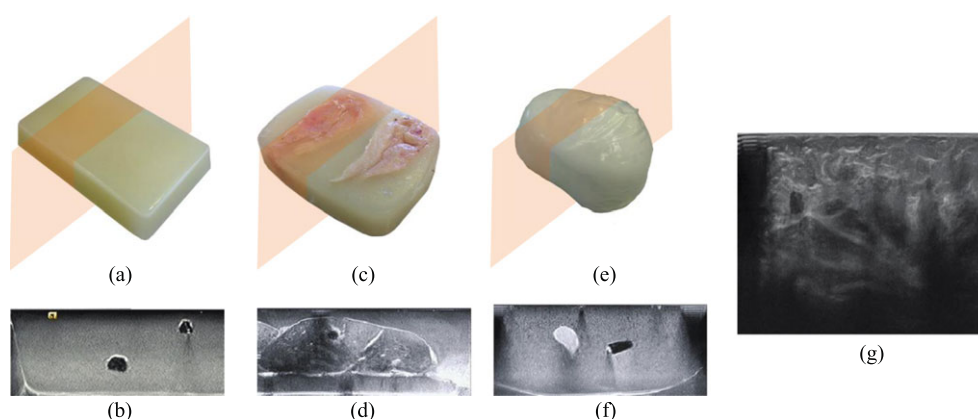
**Case IV: Clinical data:** Clinical data is also analyzed. Patient breast US image sequences were collected at Jeroen Bosch Ziekenhuis, Den Bosch, Netherlands. All subjects involved in the study were informed and consented to the use of the data in this experiment. An example US image of a patient breast is shown in Figure 8(g).

## Results

In this section, the results obtained for each one of the four cases studied are described and discussed. The statistical analysis performed on the results obtained is also described. Further, the algorithm computation time is assessed for the shapes evaluated in Case I and II.



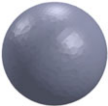
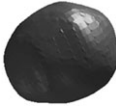


Evaluation of the obtained 3D shapes is performed comparing the results with the ground truth using DSC and MAD measures. Commercial breast phantom results are visually confirmed. Patient breast segmentation and reconstruction results are validated by an experienced clinician.

**Case I: Gelatin-based phantoms:** The reconstructed shapes are evaluated using DSC and MAD. The ground truth corresponds to the original computerized 3D drawing of the molds used to produce the object shapes. Results from the screening of several phantoms with multiple objects are shown in Table 2. Examples of 3D reconstructed objects for each of the shapes are also shown. A total of 70 cases is evaluated.



**Figure 8.** Overall view of the analyzed phantoms and slices of the respective US scans, as well as a patient breast ultrasound (US) image. (a): Gelatin phantom; (b): US slice of (a) (Gain: -12 dB, Dynamic range (DR): 55, Map: E, Space/Time (ST): 1); (c): phantom with biological tissue (chicken); (d): US slice of (c) (Gain: 0 dB, DR: 55, Map: E, ST: 1); (e): breast phantom; (f): US slice of (e) (Gain: 0 dB, DR: 55, Map: E, ST: 1); (g): patient breast US image

**Table 2** Evaluation results for seven different shapes reconstructed from gelatin-based and biological tissue phantoms. Both convex and non-convex shapes are reconstructed. The evaluated objects have vessel-like shapes (small and big), spherical shapes (small and big) and bean-like shapes (small, medium and big). Dimensions of the ground truth shapes bounding boxes are shown. Dice similarity coefficient (DSC) and mean absolute distance (MAD) mean values and standard deviations for each of the shapes are presented. Each shape is evaluated 10 times for each phantom type. The overall DSC values for gelatin phantoms and biological tissue are  $0.86 \pm 0.06$  and  $0.86 \pm 0.05$ , respectively. MAD values are  $0.30 \pm 0.09$  mm and  $0.31 \pm 0.11$  mm, in the same order

Ground truth	Reconstructed shape	Dimensions (mm)	Gelatin phantom		Biological tissue	
			DSC	MAD (mm)	DSC	MAD (mm)
		$29.43 \times 11.56 \times 4.63$	$0.76 \pm 0.04$	$0.40 \pm 0.07$	$0.77 \pm 0.04$	$0.41 \pm 0.07$
		$41.21 \times 16.18 \times 6.44$	$0.84 \pm 0.03$	$0.38 \pm 0.06$	$0.82 \pm 0.02$	$0.44 \pm 0.07$
		$\emptyset = 6$	$0.88 \pm 0.03$	$0.24 \pm 0.06$	$0.91 \pm 0.02$	$0.18 \pm 0.03$
		$\emptyset = 8$	$0.91 \pm 0.03$	$0.24 \pm 0.07$	$0.91 \pm 0.03$	$0.24 \pm 0.07$
		$10.24 \times 6.14 \times 3.62$	$0.85 \pm 0.04$	$0.29 \pm 0.08$	$0.85 \pm 0.03$	$0.28 \pm 0.05$
		$10.25 \times 12.00 \times 7.78$	$0.89 \pm 0.02$	$0.26 \pm 0.04$	$0.86 \pm 0.02$	$0.31 \pm 0.06$
		$19.19 \times 11.51 \times 6.80$	$0.92 \pm 0.02$	$0.28 \pm 0.06$	$0.88 \pm 0.03$	$0.37 \pm 0.08$

The overall DSC is  $0.86 \pm 0.06$  and MAD  $0.30 \pm 0.09$  mm. The efficiency of the segmentation is qualitatively evaluated by visually inspecting the objects contours. Examples of the segmentation results for some objects are shown in Figure 9-I.

Case II: *Biological tissue phantoms*: Examples of object segmentation in chicken phantoms are shown in Figure 9-II. Reconstruction evaluation results are shown in Table 2. A total of 70 cases is evaluated. The overall DSC is  $0.86 \pm 0.05$  and MAD  $0.31 \pm 0.11$  mm.

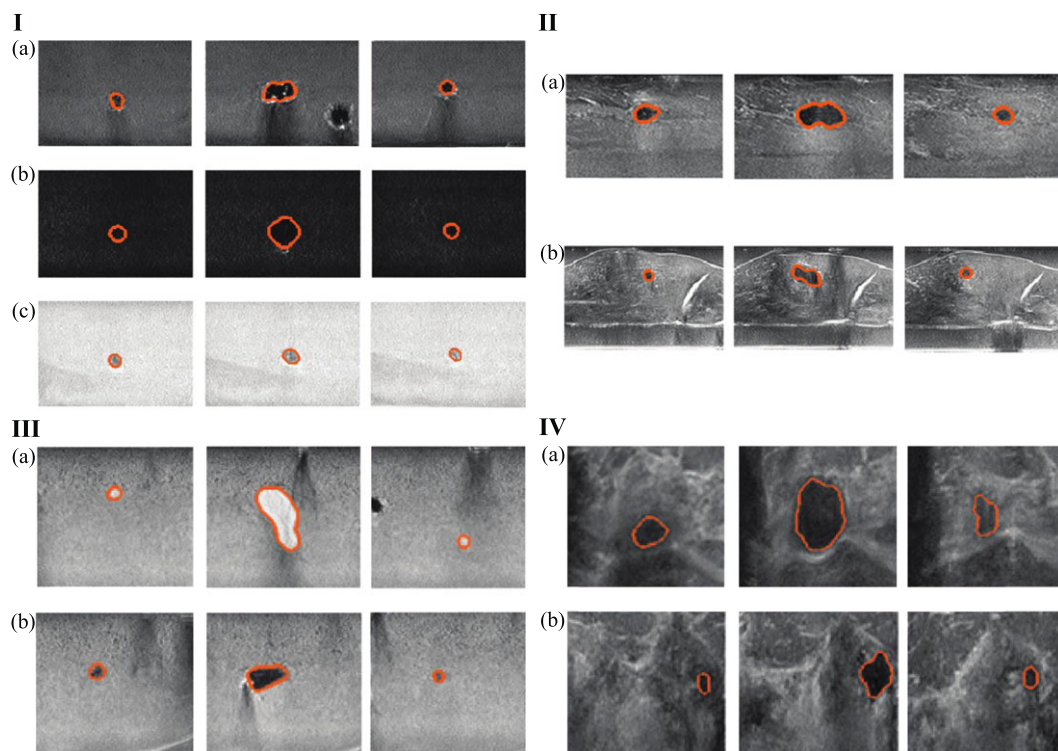


**Figure 9.** Representative segmentation performed by the algorithm. First, middle and last slices containing the objects are shown. I: gelatin phantoms: (a) object with shadow; (b) and (c) objects in both dark and bright low contrast images; II: biological tissue phantoms; III: breast phantom: (a) bright object; (b) dark object; IV: clinical data.

Case III: *Human breast phantom*: A total of 12 lesions are present in the phantom. Due to the lack of ground truth only qualitative evaluation is performed. This evaluation is done by visually confirming the contour of the object in each 2D slice. Examples of bright and dark lesion segmentations are shown in Figure 9-III and the reconstructed 3D shapes in Figure 10-II.

Case IV: *Clinical data*: US scans from six different patients are analyzed. For each patient a lesion is segmented and reconstructed. Similarly to Case III, only qualitative evaluation is performed. Lesion segmentation and reconstruction results are validated by an experienced clinician. Two examples of lesion segmentations are shown in Figure 9-IV. The reconstructed shapes of these lesions are shown in Figure 10-I. Please refer to the accompanying video that demonstrates the experiments (Electronic Supplementary Material).

*Statistical analysis*: A statistical analysis of the gelatin-based phantoms and biological tissue reconstruction results is performed to determine if they are statistically equivalent. In order to test for equivalence, the 90% confidence intervals for the difference between the two groups are evaluated. The null hypothesis that the groups differ by at least  $\varepsilon$  is rejected if the limits of the interval fall outside the  $\pm \varepsilon$  bounds. Conversely, comparability is demonstrated when the bounds of the 90% confidence interval of the mean difference fall entirely within the  $\pm \varepsilon$  bounds (60–62).

The design of equivalence tests can be challenging since the acceptance criterion  $\varepsilon$  must be defined on the basis of prior knowledge of the measurement. For a sample data set of  $p$  independent measurements with standard deviation  $\delta$ , for instance,  $\varepsilon$  must be greater than  $\delta/\sqrt{p}$ , otherwise the test may fail because of imprecision, rather than because of a true difference. Further, it must also be less than any specifications or standards that the testing is challenging, or the test will not discriminate adequately. In this work we evaluated  $\varepsilon$  as suggested in (61).

The tests revealed statistical equivalence between DSC values for gelatin phantoms and biological tissue. MAD values for these two types of data are also statistical equivalent.

*Computation time*: The computation time of the segmentation and reconstruction algorithm for a single object is assessed. Scripts are processed in a Dell Optiplex 980 desktop computer with 8.00G RAM memory and Intel®Core™i7 CPU 860@2.80GHz using MATLAB®2015a. The average computation time for the evaluated objects (Table 2) is 4.7 s, considering only the slices containing the object. The longest computation time (10 s) occurs for big vessel segmentation and reconstruction (~200 slices) and shortest (1.9 s) for the small sphere (~30 slices). A total of  $32.15 \pm 7.86$  s are needed when the entire ABVS scan (700–1030 slices) is considered.

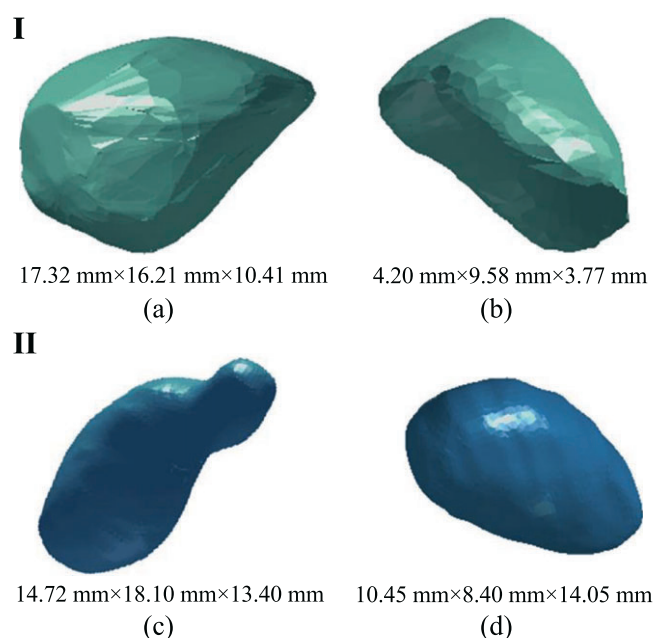


**Figure 10.** Example of reconstructed shapes of breast lesions and respective bounding box dimensions (mm). I: reconstruction of lesions from clinical data. (a) and (b) correspond to the reconstruction of the lesions shown in Figure 9-IV- (a) and (b), respectively. II: reconstruction of lesions from the breast phantom. (c) and (d) are the reconstructed shapes of the lesions shown in Figure 9-III- (a) and (b), respectively.

## Discussion

Results show that objects of significantly different sizes and shapes are accurately delineated and reconstructed in both gelatin-based phantoms (Figure 9-I) and biological tissue phantoms (Figure 9-II). Statistical analysis of the results obtained show that the algorithm works similarly for these two types of data (Table 2). This proves that the presence of biological tissue texture does not affect the algorithm's performance. The method is robust against shadowing (Figure 9-I-(a)), low contrast and different background brightness (Figure 9-I-(b) and (c)). Further, the inspection of all object 2D slices indicates that the detection of the first and last slices of the object is being correctly performed. However, DSC and MAD values are affected by the non-total correspondence between the casts and the ground truth: 1) during the fabrication process casts can retain air bubbles near their surface, affecting the reconstructed shape; 2) demolding can damage the casts, slightly altering their shape; 3) the lack of rigidity of the casts can result in shape deviations relative to the ground truth (specially noticeable in vessel-like shapes, that are elongated and thin); and 4) the objects are compressed during the scan (notice Figure 9-II-(b), where a sphere is slightly deformed).

Object segmentation in breast phantom scans visually corresponds to the expected. The wide variety of object shapes is accurately reconstructed. Segmentation and reconstruction results for patient breast US images are visually confirmed by an experienced clinician. The verification of the detected lesion contours in all the 2D slices shows that the algorithm correctly segments patient breast lesions. As the 3D reconstruction algorithm is validated using gelatin and biological tissue phantoms, the reconstructed shapes of the accurately segmented breast lesions are correct. The similarity between clinical data and biological tissue further validates the use of the algorithm for breast lesion segmentation. Lesion reconstruction enables clinicians to visually assess the 3D appearance of the tumor and retrieve the volume of the lesion. The volume plays an important role in the diagnosis assessment and can be used to trace the evolution of the state of a tumor. The GUI is a useful tool for clinicians to easily assess this information, and thus improve the diagnostic process.

## Conclusions

In this study, a method to perform segmentation and 3D reconstruction of lesions in breast-US images is proposed.

The presented algorithm does not require VOI selection and has low computation time. A GUI integrating the developed segmentation and reconstruction algorithm is also proposed. The algorithm is tested in gelatin, biological tissue (chicken) and commercial breast phantoms, as well as in clinical patient data. The evaluation of the reconstructed shapes shows that the algorithm accurately segments and 3D reconstructs lesions in the tested environments. DSC for gelatin-based phantoms is  $0.86 \pm 0.06$  and MAD is  $0.30 \pm 0.09$  mm ( $n = 70$ ). For biological tissue, DSC is  $0.86 \pm 0.05$  and MAD is  $0.31 \pm 0.11$  mm ( $n = 70$ ). Clinical patient data results are visually validated by an experienced clinician and he confirmed the segmentation and reconstruction of each lesion. Objects of different sizes, textures and shapes are detected. Both convex and non-convex objects are accurately reconstructed. The analysis of different types of data proves the robustness of the algorithm. The proposed GUI is a useful and valuable tool for clinicians to retrieve the 3D shape of a selected lesion. Lesion 3D shape and volume can be used in diagnosis. Lesion volume is of great importance for the assessment of the tumor evolution and consequent treatment adjustment. The application is also of interest to reconstruct insertion environments for needle steering. Conventional lesion localization depends on the skill of the clinician to estimate the lesion location in his mind using images, and also estimate the relative lesion position with respect to the needle. The proposed algorithm provides autonomous lesion localization that can be used for robotic needle insertion as the lesion location can be quantitatively determined, and used for autonomous needle steering.

## Future work

Future work will include testing the algorithm in a larger clinical patient database. Further, a quantitative evaluation of the algorithm in commercial breast phantom and clinical patient data will be performed. This will be achieved by obtaining the ground truth using other imaging techniques such as computerized tomography (CT) or magnetic resonance imaging (MRI). The proposed algorithm will be tested in applications other than breast lesion segmentation and reconstruction. The performance of the method will also be assessed in images acquired using other techniques, such as MRI. The algorithm will be integrated in other studies. While the algorithm potential has not yet been fully explored, the results obtained in this work are a strong validation of the method.



## Funding

This work was supported by funds from the Netherlands Organization for Scientific Research (NWO) Innovative Medical Devices Initiative (IMDI) - Project: USE (Ultrasound Enhancement).

## Conflict of Interest

The authors have declared that there is no conflict of interest.

## References

- Cheng HD, Shan J, Ju W, *et al.* Automated breast cancer detection and classification using ultrasound images: a survey. *Pattern Recog* 2010; **43**(1): 299–317.
- Rodrigues R, Braz R, Pereira M, *et al.* A two-step segmentation method for breast ultrasound masses based on multi-resolution analysis. *Ultrasound Med Biol* 2015; **41**(6): 1737–1748.
- American Cancer Society. *Breast Cancer Facts and Figs. 2013–2014*. American Cancer Society, Inc: Atlanta, 2013.
- Sivaramakrishna R, Powell KA, Lieber ML, *et al.* Texture analysis of lesions in breast ultrasound images. *Computerized Med Imag Graphics* 2002; **26**(5): 303–307.
- Cheng HD, Shi XJ, Min R, *et al.* Approaches for automated detection and classification of masses in mammograms. *Pattern Recog* 2006; **39**(4): 646–668.
- Cheng HD, Cai X, Chen X, *et al.* Computer-aided detection and classification of microcalcifications in mammograms: a survey. *Pattern Recog* 2003; **36**(12): 2967–2991.
- Devolli-Disha E, Manxhuka-Krliu S, Ymeri H, Kutllavci A. Comparative accuracy of mammography and ultrasound in women with breast symptoms according to age and breast density. *Bosn J Basic Med Sci* 2009; **9**(2): 131–136.
- Jesneck JL, Lo JY, Baker JA. Breast Mass Lesions: computer-aided diagnosis models with mammographic and sonographic descriptors. *Radiology* 2007; **244**(2): 390–398.
- Skaane P. Ultrasonography as adjunct to mammography in the evaluation of breast tumors. *Acta Radiol Suppl* 1999; **420**: 1–47.
- Stavros AT, Thickman D, Rapp CL, *et al.* Solid breast nodules: use of sonography to distinguish between benign and malignant lesions. *Radiology* 1995; **196**(1): 123–134.
- Zonderland HM, Coerkamp EG, Hermans J, *et al.* Diagnosis of breast cancer: contribution of US as an adjunct to mammography. *Radiology* 1999; **213**(2): 413–422.
- Sahiner B, Chan HP, Roubidoux MA, *et al.* Malignant and benign breast masses on 3D US volumetric images: effect of computer-aided diagnosis on radiologist accuracy. *Radiology* 2007; **242**(3): 716–724.
- Crystal P, Strano SD, Shcharynski S, Koretz MJ. Using sonography to screen women with mammographically dense breasts. *Am J Roentgenol* 2003; **181**(1): 177–182.
- Lokesh B, Shailaja K, Nanda S. Segmentation and classification of breast lesions in ultrasound images. *Int J Sci Technol Res* 2014; **3**(6).
- Noble JA, Boukerroui D. Ultrasound image segmentation: a survey. *Med Imag IEEE Trans* 2006; **25**(8): 987–1010.
- Sehgal C, Weinstein S, Arger P, Conant E. A review of breast ultrasound. *J Mammary Gland Biol Neoplasia* 2006; **11**(2): 113–123.
- Huber S, Danes J, Zuna I, *et al.* Relevance of sonographic B-mode criteria and computer-aided ultrasonic tissue characterization in differential/diagnosis of solid breast masses. *Ultrasound Med Biol* 2000; **26**(8): 1243–1252.
- Giger ML. Computer-aided diagnosis of breast lesions in medical images. *Comput Sci Eng* 2000 Sep; **2**(5): 39–45.
- Huang YL, Chen DR, Chang SC. Three-dimensional region-based segmentation for breast tumors on sonography. *J Ultrasound Med* 2012; **32**(5): 835–846.
- Chang RF, Wu WJ, Moon WK, *et al.* Segmentation of breast tumor in three-dimensional ultrasound images using three-dimensional discrete active contour model. *Ultrasound Med Biol* 2003; **29**(11): 1571–1581.
- Chen DR, Chang RF, Wu WJ, *et al.* 3-D breast ultrasound segmentation using active contour model. *Ultrasound Med Biol* 2003; **29**(7): 1017–1026.
- Horsch K, Giger M, Venta L, Vyborny C. Automatic segmentation of breast lesions on ultrasound. *Med Phys* 2001; **28**(8): 1652–1659.
- Chen DR, Chang RF, Huang YL. Computer-aided diagnosis applied to US of solid breast nodules by using neural networks. *Radiology* 1999; **213**(2): 407–412.
- Joo S, Yang YS, Moon WK, Kim HC. Computer-aided diagnosis of solid breast nodules: use of an artificial neural network based on multiple sonographic features. *Med Imag IEEE Trans* 2004; **23**(10): 1292–1300.
- Yap MH, Edirisinghe E, Bez H. A novel algorithm for initial lesion detection in ultrasound breast images. *J Appl Clin Med Phys* 2008; **9**(4).
- Yeh CK, Chen YS, Fan WC, Liao YY. A disk expansion segmentation method for ultrasonic breast lesions. *Pattern Recognition* 2009; **42**(5): 596–606.
- Madabhushi A, Metaxas DN. Combining low-, high-level and empirical domain knowledge for automated segmentation of ultrasonic breast lesions. *Med Imag IEEE Trans* 2003; **22**(2): 155–169.
- Jumaat AK, Rahman WEZWA, Ibrahim A, Mahmud R. Segmentation and characterization of masses in breast ultrasound images using active contour. In *Signal and Image Processing Applications (ICSIPA)*, 2011 IEEE International Conference on 2011; 404–409.
- Chang RF, Wu WJ, Moon W, Chen DR. Automatic ultrasound segmentation and morphology based diagnosis of solid breast tumors. *Breast Cancer Res Treat* 2005; **89**(2): 179–185.
- Huang YL, Jiang YR, Chen DR, Moon W. Level set contouring for breast tumor in sonography. *J Digital Imag* 2007; **20**(3): 238–247.
- Boukerroui D, Baskurt A, Noble JA, Basset O. Segmentation of ultrasound images - multiresolution 2D and 3D algorithm based on global and local statistics. *Pattern Recog Lett* 2003; **24**(4-5): 779–790.
- Xiao G, Brady M, Noble JA, Zhang Y. Segmentation of ultrasound B-mode images with intensity inhomogeneity correction. *Med Imag IEEE Trans* 2002; **21**(1): 48–57.
- Gómez W, Leija L, Alvarenga A, *et al.* Computerized lesion segmentation of breast ultrasound based on marker-controlled watershed transformation. *Med Phys* 2010; **37**(1): 82–95.
- Zhang L, Ren Y, Huang C, Liu F. A novel automatic tumor detection for breast cancer ultrasound Images. In *Fuzzy Systems and Knowledge Discovery (FSKD)*, 2011 8th International Conference on. vol. 1; 2011; 401–404.
- Drukker K, Giger M, Horsch K, *et al.* Computerized lesion detection on breast ultrasound. *Med Phys* 2002; **29**(7): 1438–1446.
- Dokur Z, Olmez T. Segmentation of ultrasound images by using a hybrid neural network. *Pattern Recog Lett* 2002; **23**(14): 1825–1836.
- Su Y, Wang Y, Jiao J, Guo Y. Automatic detection and classification of breast tumors in ultrasonic images using texture and morphological features. *Open Med Info J* 2011; **5**: 26–37.
- Shan J, Cheng HD, Wang Y. Completely automated segmentation approach for breast ultrasound images using multiple-domain features. *Ultrasound Med Biol* 2012; **38**(2): 262–275.
- Liu B, Cheng HD, Huang J, *et al.* Fully automatic and segmentation-robust classification of breast tumors based on

- local texture analysis of ultrasound images. *Pattern Recog* 2010; **43**(1): 280–298.
40. Kuo HC, Giger ML, Reiser I, et al. Segmentation of breast masses on dedicated breast computed tomography and three-dimensional breast ultrasound images. *J Med Imag* 2014; **1**(1): 014501.
  41. Ye C, Vaidya V, Zhao F. Improved mass detection in 3D automated breast ultrasound using region based features and multi-view information. In International IEEE Conference on Engineering in Medicine and Biology Society (EMBC); 2014; 865–2868.
  42. Chang WL, Chang CC, Chen WM. Computer-aided diagnosis system for variance estimation of 3D ultrasonography based on gabor filter. In International Conference on Biomedical Engineering and Computer Science (ICBECS); 2010; 1–4.
  43. Abayazid M, Moreira P, Shahriari N, et al. Ultrasound-guided three-dimensional needle steering in biological tissue with curved surfaces. *Med Eng Physics* 2015; **37**(1): 145–150.
  44. Singh HK, Tomar SK, Maurya PK. Article: Thresholding Techniques applied for Segmentation of RGB and multispectral images. IJCA Proceedings on National Conference on Advancement in Electronics and Telecommunication Engineering. 2012; NCAETE(1); 24–27.
  45. Davies ER. Machine Vision: Theory, Algorithms, Practicalities. Academic Press (1990).
  46. Edelsbrunner H, Mücke EP. Three-dimensional alpha shapes. *ACM Trans Graph* 1994; **13**(1): 43–72.
  47. Desbrun M, Meyer M, Schröder P, Barr AH. Implicit Fairing of Irregular Meshes Using Diffusion and Curvature Flow. In Proceedings of the 26th Annual Conference on Computer Graphics and Interactive Techniques; 1999; 317–324.
  48. Belyaev A. Mesh smoothing and enhancing; 2013. Available from: <http://goo.gl/EByt7o>.
  49. Kroon DJ. Smooth Triangulated Mesh; 2010. Available from: <http://www.mathworks.com/matlabcentral/fileexchange/26710-smooth-triangulated-mesh>.
  50. Besl PJ, McKay ND. A method for registration of 3-D shapes. *IEEE Trans Pattern Anal Machine Intell* 1992; **14**(2): 239–256.
  51. Castellani U, Bartoli A. 3D shape registration. In 3D Imaging, Analysis and Applications, Springer, 2012.
  52. Dice LR. Measures of the amount of ecologic association between species. *Ecology* 1945; **26**(3): 297–302.
  53. Aspert N, Santa-Cruz D, Ebrahimi T. MESH: Measuring Errors between Surfaces using the Hausdorff Distance. In Proc. of the IEEE International Conference in Multimedia and Expo (ICME); Vol. 1; 2002; 705–708.
  54. Gerig G, Jomier M, Chakos M. Valmet: A New Validation Tool for Assessing and Improving 3D Object Segmentation. In *Medical Image Computing and Computer-Assisted Intervention - MICCAI 2001*, Vol. **2208**. Springer Berlin Heidelberg, 2001; 516–523.
  55. Abayazid M, Roesthuis RJ, Rob Reilink SM, Misra S. Integrating deflection models and image feedback for real-time flexible needle steering. *IEEE Trans Robotics* 2013; **29**(2): 542–553.
  56. Madsen E, Zagzebski J, Banjavie R, Jutila R. Tissue mimicking materials for ultrasound phantoms. *Med Phys* 1978; **5**(5): 391–394.
  57. Cook JR, Bouchard RR, Emelianov SY. Tissue-mimicking phantoms for photoacoustic and ultrasonic imaging. *Biomed Opt Express* 2011; **2**(11): 3193–3206.
  58. Hall TJ, Bilgen M, Insana MF, Krouskop TA. Phantom materials for elastography. *IEEE Trans Ultrason, Ferroelect, Frequency Control* 1997; **44**(6): 1355–1365.
  59. Ryan LK, Foster FS. Tissue equivalent vessel phantoms for intravascular ultrasound. *Ultrasound Med Biol* 1997; **23**(2): 261–273.
  60. Chen C, Rathore N, Ji W, Germansderfer A. Statistical equivalence testing for assessing bench-scale cleanability. *BioPharm Int* 2010; **23**(2): unpagged.
  61. Limentani GB, Ringo MC, Ye F, Bergquist ML, McSorley EO. Beyond the t-test: statistical equivalence testing. *Anal Chem* 2005; **77**(11): 221–226.
  62. Pacchierotti C, Prattichizzo D, Kuchenbecker KJ. Displaying sensed tactile cues with a fingertip haptic device. *IEEE Trans Haptics* 2015; **8**(4): 384–396.

## Supporting information

Supporting information may be found in the online version of this article.